© 2016. Published by The Company of Biologists Ltd | Journal of Cell Science (2016) 129, 245-255 doi:10.1242/jcs.152272

COMMENTARY

ARTICLE SERIES: IMAGING

Third harmonic generation microscopy of cells and tissue organization

Bettina Weigelin[1], Gert-Jan Bakker[1] and Peter Friedl[1,2,3,*]

ABSTRACT

The interaction of cells within their microenvironmental niche is fundamental to cell migration, positioning, growth and differentiation in order to form and maintain complex tissue organization and function. Third harmonic generation (THG) microscopy is a label-free scatter process that is elicited by water-lipid and water-protein interfaces, including intra- and extracellular membranes, and extracellular matrix structures. In applied life sciences, THG delivers a versatile contrast modality to complement multi-parameter fluorescence, second harmonic generation and fluorescence lifetime microscopy, which allows detection of cellular and molecular cell functions in three-dimensional tissue culture and small animals. In this Commentary, we review the physical and technical basis of THG, and provide considerations for optimal excitation, detection and interpretation of THG signals. We further provide an overview on how THG has versatile applications in cell and tissue research, with a particular focus on analyzing tissue morphogenesis and homeostasis, immune cell function and cancer research, as well as the emerging applicability of THG in clinical practice.

KEY WORDS: Multiphoton microscopy, Third harmonic generation, Nonlinear imaging

Introduction

The visualization of living cells within their tissue environment is a central endeavor and challenge in life sciences. Besides chemical and molecular labels to generate contrast of defined molecular structures, and to allow visualization of cells in three dimensions and over time, nonlinear microscopy enables label-free visualization of cell and tissue structures (Alexander et al., 2013; Ellenbroek and van Rheenen, 2014; Helmchen and Denk, 2005). Originally used in material sciences, the development of high-power lasers, optimized objective design and high-sensitivity photomultipliers with a wide dynamic range have recently enabled the application of third harmonic generation (THG) microscopy to three-dimensional (3D) cell and tissue microscopy, which complements broadly used fluorescence and second harmonic generation (SHG) detection. We here review the principles and live-cell applications of THG microscopy, which together with SHG and fluorescence detection enables powerful 3D visualization of the extracellular matrix, cell morphology and subcellular organization for multi-parameter analysis of cell–tissue interaction and function.

[1]Department of Cell Biology, RIMLS, Radboud University Medical Center, Nijmegen, 6525 GA, The Netherlands. [2]David H. Koch Center for Applied Research of Genitourinary Cancers, Department of Genitourinary Medical Oncology, The University of Texas MD Anderson Cancer Center, Houston, TX 77030, USA. [3]Cancer Genomics Centre, The Netherlands.

*Author for correspondence (peter.friedl@radboudumc.nl)

Physical principles of THG

Higher harmonic generation is a nonlinear coherent scattering process, resulting from phase matching and summation of light waves that are induced by inorganic and organic structures that have specific physical properties, molecular arrangement and order. SHG results from the conversion of two incoming photons into one emitted photon with doubled energy and thus, the emission of light of half the wavelength (Fig. 1A,B). SHG occurs at ordered non-centrosymmetric structures that are found predominantly in metals and crystals (Chen et al., 2008; Chu et al., 2002). Likewise, biological materials contain large-scale repetitive non-centrosymmetric units – including coiled-coil structures and polymeric proteins, which facilitate SHG signals, for instance at striated muscle and fibrillar collagen (Campagnola et al., 2002; Friedl et al., 2007). THG results from the tripling of the frequency of the excitation wavelength, whereby the combined energy of three photons is converted into one emitted photon with one third of the excitation wavelength and tripled energy (Barad et al., 1997) (Fig. 1A,B). THG occurs at structural interfaces, such as local transitions of the refractive index or the third-order nonlinear susceptibility χ^3 (Barad et al., 1997; Müller et al., 1998), which are both intrinsic physical properties of materials and liquids. Therefore, THG is more versatile compared to SHG because it does not require a specific asymmetry of the structure to be imaged. In tissues, THG excitation occurs predominantly at interfaces that are formed between aqueous interstitial fluids and lipid-rich structures, such as cellular membranes (Aptel et al., 2010; Rehberg et al., 2011), lipid droplets (Débarre et al., 2006; Tserevelakis et al., 2014; Watanabe et al., 2010), or inorganic structures, such as calcified bone or enamel in teeth (Chen et al., 2008; Oron et al., 2004). In addition, THG can also be found at interfaces between water and large protein aggregates, such as collagen bundles or muscle fibers (Rehberg et al., 2011; Weigelin et al., 2012).

Technical and experimental considerations of THG application

Determinants of signal intensity

The signal intensity of THG crucially depends on the size and organization of the signal-eliciting structures at the micrometer scale (Fig. 1E), the excitation and detection approach (Fig. 1C,D), and both power and polarization of the incident light. Although no signal is obtained in homogeneous dispersed medium, the signal is elicited by interfaces (Fig. 1E, examples 5 and 6) and optical inhomogeneities of length scales that are comparable to the focal volume of the laser beam (Cheng and Xie, 2002; Débarre et al., 2005) (Fig. 1E, examples 1–4). Consequently, the THG signal intensity is strongly affected by the size of the structure and the resolution of the system, notably the numerical aperture of the objective. Tuning of the focal volume can thus be used to optimize THG intensity for specific structures of interest. In *Drosophila* embryos for example, tightening the focus enhances the signal from the external membrane (a scenario comparable to that in Fig. 1E, example 6), whereas, when

Journal of Cell Science (2016) 129, 245-255 doi:10.1242/jcs.152272

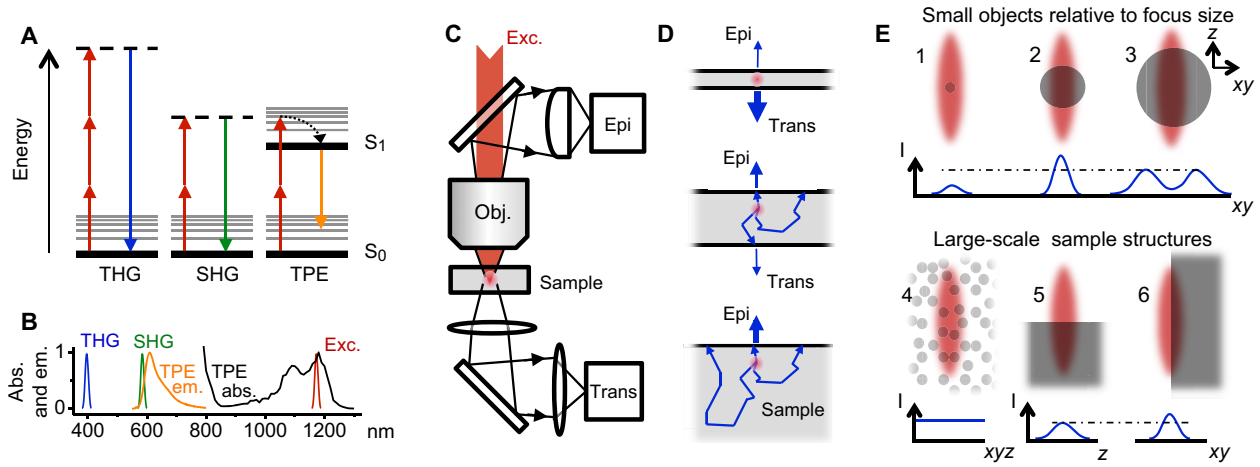

Fig. 1. Principles of THG signal generation. Excitation (Exc.) is shown in red and other colors refer to emission. (A) Jablonsky diagram of THG, SHG and two-photon fluorescence excitation (TPE). Excitation with the same wavelength results in signals of a distinct emission wavelength. Dashed lines, virtual states. S_0 and S_1, ground-level and first-excited electron state, respectively, with vibrational levels (thin lines). (B) Absorption (abs.) and emission (em.) spectra of THG, SHG and two-photon excitation (mCherry is shown here), excited with 1180-nm light and scaled to maximum absorption and emission. (C) Scheme of the experimental setup of a multiphoton microscope equipped for detection of epi (backward) and trans (forward) signals. Red dot, focal volume. The excitation light is focused though the objective (Obj.) lens on the sample, and the epi-signal is picked up by the objective, reflected by a semi-transparent mirror and collected by an ultrasensitive photomultiplier (typically a gallium arsenide phosphide detector). The trans-signal is collected by a condenser lens below the sample and focused onto a photomultiplier. (D) Sample thickness determines the relative strength of epi versus trans THG signals (blue arrows). In thin samples, THG is optimally detected in the trans direction (upper scheme), owing to the lack of scattered THG signals. With increasing sample thickness and scattering, photon frequency below the samples diminishes, but increases in the epi direction (middle and lower schemes). (E) Axial (*z*) and lateral (*xy*) THG intensity ('I') profiles (blue line) depend on the object (gray) size and orientation with respect to the excitation focus (red). Small round objects (top, 1–3) yield a maximum signal strength if their size is in the order of the focal volume of the excitation beam (compare the maxima of intensity profiles in scenarios 1–3 in reference to the dotted line). Larger objects yield maxima at the interfaces of the object with the surrounding medium. Random distribution of small inhomogeneities in a relatively large focal volume generates a continuous THG signal in all directions (4) (e.g. dense gray matter in the cortex of the brain; or internal organelles in a *Drosophila* embryo). Horizontal and vertical discontinuities (shaded boxes) within the focus induce strong THG signals at the transition (5 and 6). Here, a vertical discontinuity generates a stronger signal compared to a horizontal interface.

using a weakly focused beam, signals predominantly originate from densely packed internal micrometer-sized organelles (Débarre et al., 2005; Mahou et al., 2011) (a scenario comparable to that in Fig. 1E, example 4). THG signal strength and origin further depend on the orientation of the interface within the focal volume, with an optimal THG signal generated by an interface orientation that is parallel to the excitation beam (Cheng and Xie, 2002; Müller et al., 1998) (Fig. 1E, examples 5 and 6). Lastly, THG signals are sensitive to the polarization of the excitation light (Oron et al., 2004); in human cornea, using a circularly polarized excitation beam allows the specific detection of interfaces of the lamellae, whereas a linear polarized excitation beam reveals stromal keratocytes and epithelial cell boundaries (Aptel et al., 2010). Thus, signal intensity strongly depends on local imaging conditions.

Excitation wavelengths

In principle, THG is generated at any wavelength of light. Practically, the optimal excitation wavelength is determined by a trade-off between tissue scattering and absorption. THG detection in the UV range is precluded owing to a strong scattering and absorption of UV light by tissues, and the lack of UV transmission by most optical glasses. The optimal excitation window is determined by a trade-off between tissue scattering and water absorption of the laser light. Longer wavelengths reduce scattering, but light with a wavelength above 1350 nm is more strongly absorbed by water, which limits tissue penetration. By contrast, in brain tissue for example, wavelengths in the spectral excitation window of 1700 nm provide optimal THG imaging depths of up to ~1 mm (stratum pyramidale) (Horton et al., 2013).

In practice, infrared excitation (wavelength range 1180–1350 nm) and detection within the lower blue spectrum (390–450 nm) is best suited to generate and detect THG using with the same objective lens. Detecting THG in the blue range further has the advantages of minimum spectral overlap and convenient combination with commonly used cyan, green and red fluorophores, as well as SHG in the green–yellow range (compare examples in Figs 1 and 2).

Laser-power range

THG as a third-order process is strongly reactive to alteration of excitation power density in the focus – i.e. a twofold increase of laser power results in an eightfold increase in THG signal intensity. Thus, a modest increase in excitation power will substantially improve the THG signal. Conversely, even only a small loss of photon density in the focus will result in a substantial loss of THG signal. Further, signal intensity strongly depends on excitation pulse length and laser repetition rate (with both inverse second-order dependence), excitation wavelength (third-order dependence) and the numerical aperture of the objective (second-order dependence) (Cheng et al., 2014). In deep-tissue imaging applications, THG signals are thus strongly affected by light scattering and wavelength dispersion that is caused by out-of-focus structures and by increasing distortions of the focus in depth (Dietzel et al., 2014). The detection of THG in 3D tissues can be improved by using adaptive optics in order to achieve a sharp focus in light-scattering samples, which maximizes the signal intensity of SHG and THG (Thayil et al., 2011). Further, THG signal strength benefits from pulse predispersion compensation, to counteract pulse dispersion by the optical components and the sample itself (McConnell, 2006). Because of this nonlinearity and sensitivity to even small changes of imaging conditions, conclusions that are based on THG intensity could be problematic.

Journal of Cell Science (2016) 129, 245-255 doi:10.1242/jcs.152272

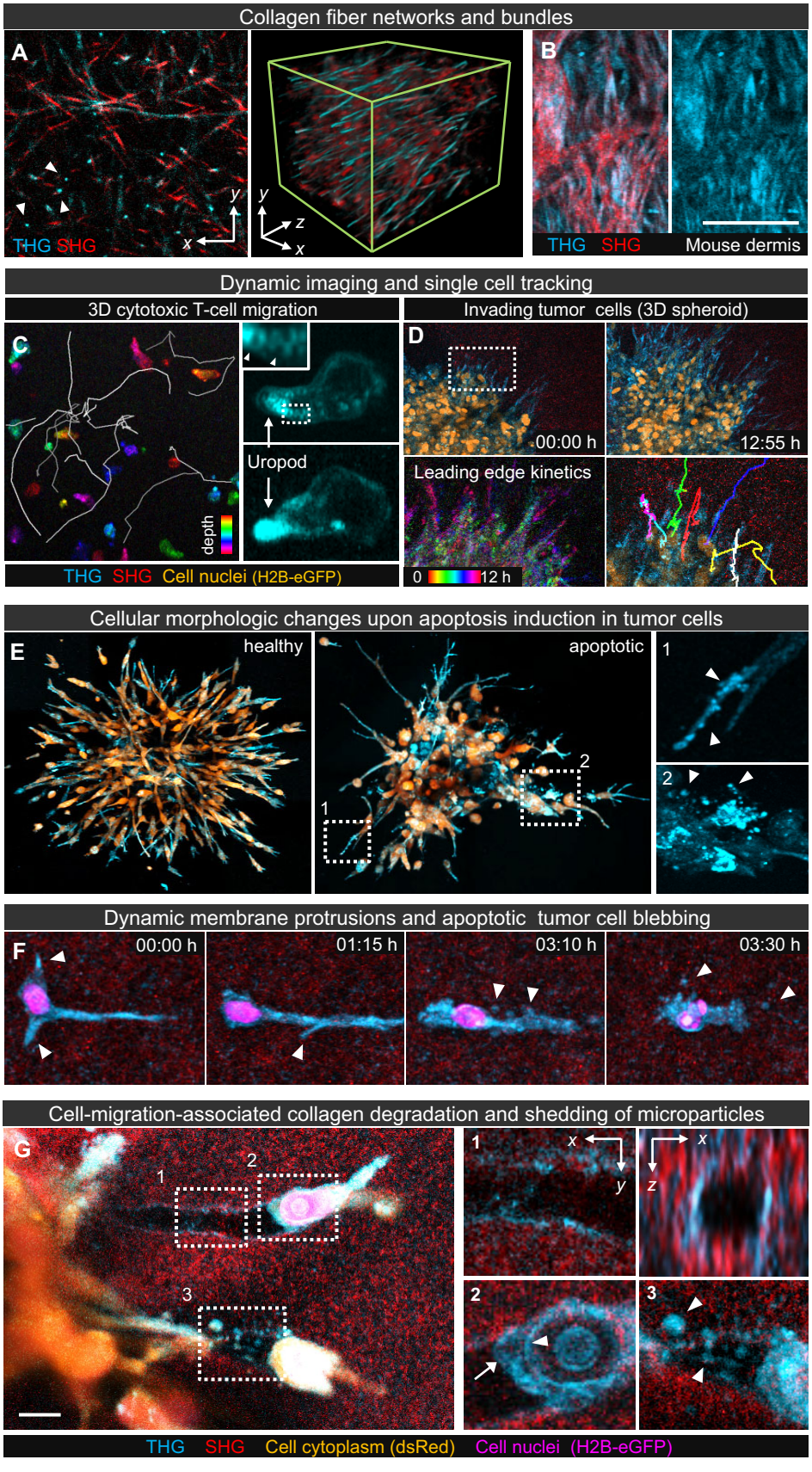

Fig. 2. THG imaging *in vitro*. Unless indicated otherwise, forward detection was used in the examples shown. (A) Complementary SHG and THG signal of 3D fibrillar collagen. Compared to SHG, THG signals generated by collagen fibers originate from the fiber surface and are usually weaker in intensity. As an exception, a strong THG signal originates from fibers that are oriented parallel to the excitation laser beam. The THG signal is visible as spots in the *xy* plane (arrowheads in the left image) and appears as fibers in the *z*-reconstruction of the fiber cross section (shown on the right). THG thereby detects fibers that are invisible with SHG detection alone. (B) SHG and THG signals from thick collagen fiber bundles in the mouse dermis (backward detection). Scale bar: 100 µm. (C) Time-lapse recording of cytotoxic T cells migrating in 3D collagen matrix. The position of cells in the *z*-direction is color-coded as indicated. White lines represent migration tracks within a 60-min period. The zoom images and insets show a single cytotoxic T cell and a uropod containing intracellular vesicles (indicated by arrowheads). (D) Dynamic imaging of fibrosarcoma cells invading into 3D collagen matrix. THG and individual cell tracks show the dynamics of the leading edge. (E) Monitoring cell morphology and subcellular membrane kinetics upon apoptosis induction. HT1080 human fibrosarcoma tumor cell spheroids were incubated for 24 h without (healthy) or with Etoposide (apoptotic) and imaged by using THG. Zoom sections highlight the subcellular resolution and the level of detail that can be achieved with THG imaging, including membrane blebs during early apoptosis (zoom 1, arrowheads) and apoptotic microparticles after cell fragmentation (zoom 2, arrowheads). (F) Time-lapse recording of dynamic membrane protrusions and apoptotic membrane blebbing of an HT1080 cell. Low phototoxicity of the infrared excitation and lack of bleaching of the THG signal allow dynamic reconstructions of cellular processes at subcellular resolution over extended time periods compared to fluorescence imaging. (G) Proteolytic tracks formed by HT1080 cells invading into 3D collagen matrix. Strong THG signals (cyan) originate from the linear track interface (zoom 1), cellular (arrow) and nuclear (arrowhead) membranes (zoom 2), and microvesicles (zoom 3, arrowheads). Complementary to fluorescence labeling and SHG, THG offers label-free detection of subcellular morphological features and detects the reorganization of extracellular matrix interfaces; here, tissue microtracks are generated by proteolytically active migrating cells. Cytoplasmic dsRed2 signal is shown in orange, nuclear histone-2B–eGFP is labeled magenta and the SHG signal of collagen is red. Excitation – THG, SHG and dsRed, 1180 nm, 100 mW; GFP, 910 nm, 20 mW. Scale bar: 20 µm.

Phototoxicity

In contrast to fluorescence, THG is an energy-conserving process whereby the emitted photon contains the total energy of three exciting photons, and no energy is absorbed by the signal-eliciting structures (Squier et al., 1998). Therefore, THG causes neither photobleaching nor generation of reactive oxygen

Journal of Cell Science (2016) 129, 245-255 doi:10.1242/jcs.152272

species. In addition, owing to the lack of out-of-focus excitation, any photodamage caused by THG imaging in 3D tissue samples is confined to the scanned volume. However, the high illumination power required for THG can induce tissue damage. Independent from the THG process, phototoxic molecules can be generated by concurrent two- and three-photon (auto)fluorescence excitation, reabsorption of THG emission or thermal damage through tissue absorption of excitation light (Débarre et al., 2014). These indirect effects typically require careful choice of excitation wave length (typically 1200 nm and higher), because phototoxic effects are significantly reduced with longer wavelengths (Andresen et al., 2009; Chen et al., 2002). For imaging of zebrafish embryos, wavelengths in the range of 1200–1300 nm do not seem to generate photodamage and have been proven to be suitable for the repeated scanning that is required for long-term time-lapse imaging (Sun et al., 2004; Chu et al., 2003).

Forward and backward detection

According to the momentum conservation law, the generated higher harmonic photons are mostly emitted in the same direction as the initiating photons, thus the emission light propagates in a forward direction, away from the objective (Cheng and Xie, 2002) (Fig. 1C). Therefore, THG signals from transparent samples are best detected with forward detectors mounted on the side of the sample that is opposite to the exciting laser beam. In non-transparent samples, scattering of the THG signal allows backward (epi-)detection of photons, which are backscattered by the tissue (Débarre et al., 2006). Consequently, the intensity of epi-THG signals improves in dense scattering tissue and media where more forward-generated THG photons are backscattered (Débarre et al., 2007; Rehberg et al., 2011) (Fig. 1C). In addition, theoretical studies and experimental evidence of nanoparticles in aqueous solution suggest that a direct backward component of THG exists, in addition to the photons that are indirectly scattered from forward THG (Chang et al., 2010a). Generally, backward THG appears as a weak forward THG signal with a decreased signal-to-noise ratio, and the same structures can be detected (Rehberg et al., 2011; Tai et al., 2005). There are only a few reports of exceptions of differing forward:backward intensity ratios for specific structures, such as striated muscle, nuclear chromocenters (Rehberg et al., 2011) and collagen fiber cross sections (our own observation). Because of the weakness of THG, particularly in detection of backward scatter, high-sensitivity detectors, such as gallium arsenite phosphide (GaAsP) photomultipliers are required.

THG in biological samples, in comparison to multiphoton and confocal fluorescence imaging

For use in life sciences, THG has several unique technical and application advantages. In contrast to multiphoton and confocal fluorescence imaging, THG is readily detected without the need for tissue staining and delivers a broad range of structural information on cell and tissue architecture. Similar to multiphoton excitation, and in contrast to one-photon confocal imaging, THG is only generated in the focal volume; therefore, the imaging process and signals that are detected are intrinsically confocal and suited for scanning of 3D samples and for the reconstruction of their volume. Confocal imaging is limited to the superficial cell layers of tissues owing to scattering, absorption and phototoxicity limitations, whereas the infrared wavelengths that are used for multiphoton and THG excitation allow long-term time-lapse imaging (Fig. 2C,D,F; Sun et al., 2004) and facilitate deep-tissue penetration (Andresen et al., 2009). Similar to optical coherence tomography (OCT) and ultrasound, but in contrast to other label-free imaging modalities – including coherent anti-Stokes Raman scattering (CARS) and autofluorescence – THG provides structural but not molecular information (Box 1). Thus, THG is complementary to other imaging approaches and is best applied within multi-parameter acquisition schemes.

Box 1. Label-free imaging modalities in life sciences

Label-free imaging modalities generate image contrast by exploiting intrinsic material, structural or chemical properties of the sample.

In optical coherence tomography and microscopy (OCT and OCM, respectively), a 3D image is reconstructed based on variations in the time-delay and scattering pattern of the excitation light, which is reflected by tissue structures and interfaces. OCT creates contrast in a similar manner to that of ultrasound; however, by using light instead of the long wavelengths of sound or radio frequency, it achieves higher resolution. OCT provides images of large fields of view in real-time with several millimeters of penetration depth while typically maintaining lateral and axial resolution in the micrometer range. Similar to THG, OCT provides structural but not molecular contrast. When combined with Doppler imaging for label-free micro-angiography, OCT delivers powerful structure–function insight into, for example, blood flow (Drexler et al., 2014). Photoacoustic imaging uses excitation by laser light, which is absorbed by tissue and partially converted into heat; this leads to ultrasonic emission, which is detected for image reconstruction (Beard, 2011). Thus, the high contrast of photo-absorption is combined with the low scattering properties of ultrasound (Zhang et al., 2015). Optical absorption properties of tissue components vary with physiological conditions, such as hemoglobin concentration and oxygen saturation, and this can be exploited, for instance, for quantitative measurements of blood oxygen saturation. The current resolution of photoacoustic imaging is in the range of approximately 100 µm, but can be improved to cell-level resolution by combining photoacoustic imaging with microscopy (PAM) (Zhang et al., 2015). Compared to photoacoustic imaging, the penetration depth of PAM is reduced from several millimeters to less than 1 mm. OCT and OCM, ultrasound and photoacoustic techniques provide fast image acquisition, large imaging depths, but (supra)cellular resolution. In contrast, optical modalities such as two photon autofluorescence (AF), SHG, THG and coherent anti-Stokes Raman scattering (CARS) provide sub-cellular resolution with added structural and molecular specificity. SHG and THG detect frequency changes of the tissue-scattered excitation light, such as frequency doubling (SHG) and tripling (THG), which occurs at structures of particular asymmetry (SHG) or optical interfaces (THG) using a single laser beam. For CARS, a pump beam and a Stokes beam interact with each other and the sample in a wave-mixing process, and thereby enable molecular vibrational spectroscopy of the sample. CARS can distinguish tissue structures based on their chemical composition, such as DNA, lipid, metabolite or protein content (Evans and Xie, 2008). Compared to CARS, THG produces high-contrast images that are rich in detail with a much simpler excitation scheme and minimal risk for aberration artifacts that are induced by the mixing of two excitation beams. Conversely, CARS provides information on the chemical properties of cell and tissue structures. Alternatively, label-free molecular contrast can originate from tissue autofluorescence. By analyzing the spectroscopic properties of the emission – e.g. by using fluorescence lifetime imaging (FLIM) or spectral imaging – multiple signals originating from, for example, NADH, flavins, retinol, keratin, FAD, melanin and elastin can be separated and quantified (Fereidouni et al., 2014; Skala et al., 2007; Zipfel et al., 2003). Compared to THG, autofluorescence signals require shorter near infra-red excitation wavelengths and usually have a low signal-to-noise ratio, which limits detection in scattering tissues. Two-photon-excited autofluorescence, SHG, THG and CARS can be easily combined with multiphoton fluorescence microscopy on the same platform, using the same laser source. Each modality adds distinct structural and/or chemical context to the fluorescence data.

Journal of Cell Science

Table 1. Overview of tissue structures that can be visualized with THG, and imaging applications

Visualized structure	Tissue	Biological application and comments	Reference
Extracellular matrix and inorganic structures			
Collagen fibers and bundles	Mouse skin; mouse cremaster muscle	3D reconstruction of tissue organization and interstitial space, cell–matrix interaction and guidance; signal originates from the fiber surface, complementary to SHG	Rehberg et al., 2011; Weigelin et al., 2012; Wu et al., 2015; Fig. 2A,B,G
Elastic fibers	Human conjunctiva	Signal originates from the fiber surface, complementary to SHG; shows disease-related proliferation of elastic fibers	Sun et al., 2007
Basement membranes	Mouse cremaster muscle, ear, dermis	Visualization of delineating vessels and muscle fibers, likely to represent the surface signal that results from the interface between the basement membrane and stroma or adherent cells	Dietzel et al., 2014; Rehberg et al., 2011; Weigelin et al., 2012
Mineralized bone matrix	Mouse embryonic bone	Surface signal; visualization of mineralized bone matrix	Oron et al., 2004
Calcified teeth	Human teeth; fossil vertebrate teeth	Detection of cracks or lesions resulting from mineral loss; classification of fossil vertebrate teeth	Chen et al., 2008; Chen et al., 2015b; Kao, 2004
Cells, cellular membranes and cell organelles			
Cellular membranes	Human cornea and skin; zebrafish embryo	Visualization of tissue architecture and abnormalities during disease; cell lineage tracing during embryo development	Aptel et al., 2010; Chen et al., 2009; Tsai et al., 2014; Olivier et al., 2010a,b
Nuclear membrane, nucleoli	Mouse cremaster muscle, human oral mucosa and skin	Visualization of abnormalities during disease; nuclear morphology changes during cell proliferation and death; analysis of the nucleocytoplasmic ratio to detect malignant lesions	Rehberg et al., 2011; Tsai et al., 2011; Fig. 2G
Adipocytes	Mouse cremaster muscle, dermis, human epicardial adipose tissue	Identification of the 3D organization and interfaces present in fat tissue, used to understand cell invasion into fat tissue; exploited for intraoperative assessment of cardiovascular risk factors based on adipocyte size and distribution	Tsai et al., 2013; Weigelin et al., 2012
Erythrocytes	Arterial and venous vessels, interstitial tissue after hemorrhage, whole-blood *ex vivo*	Hematological analysis of blood flow dynamics, erythrocyte:leukocyte ratios, stasis or turbulence; flow-based assessment of heart rate; detection of malaria infection	Bélisle et al., 2008; Chen and Liu, 2012; Dietzel et al., 2014
Leukocytes	Mouse ear, cremaster muscle	Detection of leukocyte infiltration into tissues during disease; identification of leukocyte subsets; leukocyte polarity	Rehberg et al., 2011; Tsai et al., 2012; Fig. 2C
Microvesicles	Mouse melanoma	Visualization of oncogenic conditioning of the tumor microenvironment; kinetics of microvesicle distribution in tissue	Weigelin et al., 2012; Fig. 2G and 3F,I
Intracellular vesicles and lipid bodies	Mouse hepatocytes, *C. elegans* and mouse embryo	Monitoring of lipid metabolism and lipid body dynamics	Débarre et al., 2006; Tserevelakis et al., 2014; Watanabe et al., 2010
Striated muscle	Mouse dermis, cremaster muscle	Detection of I-bands complementary to the SHG signature; identifies muscle as a 3D guiding structure for tumor cell migration	Rehberg et al., 2011; Weigelin et al., 2012
Axons and neurons	Mouse brain, spinal cord	Dynamic monitoring of myelin organization and degeneration; orientation during image-guided brain surgery	Farrar et al., 2011; Lim et al., 2014; Witte et al., 2011

Higher harmonic generation in life sciences – from humble beginnings to state-of-the-art clinical applications

Shortly after the first laser was developed, the principles and first applications of higher harmonic generation were established, and SHG was demonstrated by Peter A. Franken in 1961 by focusing the laser through crystalline quartz (Franken et al., 1961). In 1997, the first THG microscope was developed that demonstrated the applicability of THG generation by interfaces and inhomogeneities in three dimensions (Barad et al., 1997). THG was first used in applied physics to detect laser-induced breakdown in glass (Squier et al., 1998) and liquid crystal structures (Yelin et al., 1999). The first biological applications included 3D reconstructions of plant leaves, live neurons, organelles in yeast and statolith movement in rhizoid cells, which demonstrated that THG can be used to visualize structures and dynamics in live-cell culture and tissues without the need for any exogenous labeling (Müller et al., 1998; Squier et al., 1998; Yelin and Silberberg, 1999). Initial biological applications of THG prioritized the imaging of transparent objects and the detection of THG signals in the forward direction – e.g. to track single-cell and tissue movements in early-stage embryos (Débarre et al., 2004; Sun

Journal of Cell Science (2016) 129, 245-255 doi:10.1242/jcs.152272

et al., 2004). Over the past decade, THG microscopy has evolved from proof-of-principle studies towards a valuable tool in life science research, tissue morphogenesis and disease progression, with the potential for clinical application in optical biopsies (Table 1).

THG imaging of cells, cellular membranes and cell organelles

Cellular tissue architecture and composition

Cellular membranes, including the cell membrane, nuclear membrane and intra- and extracellular vesicles, are an abundant source of THG signals (Zimmerley et al., 2013) (Fig. 2C–G; Movies 1–4). In intact epithelia, such as mouse and human skin, THG has been used to reveal the morphology, size and distribution of epidermal and dermal cells, such as keratinocytes, adipocytes (Fig. 3E) and infiltrating leukocytes with sub-micron spatial resolution (Tai et al., 2005; Weigelin et al., 2012). Likewise, in human cornea, THG has been used to visualize epithelial cell boundaries and corneal keratocyte networks, which has helped to monitor keratocyte migration and activation during haze formation and corneal allograft wound healing (Aptel et al., 2010; Olivier et al., 2010a). In tissue-engineered corneas, combined SHG and THG imaging has recently been used to provide noninvasive quality control measurements of cornea thickness, of collagen structure, and of the distribution and density of stromal fibroblasts and endothelial cells (Jay et al., 2015).

Similarly, the position and migration of leukocytes infiltrating the mouse cremaster muscle and the mouse ear have been readily detected by using THG microscopy (Rehberg et al., 2011; Tsai et al.,

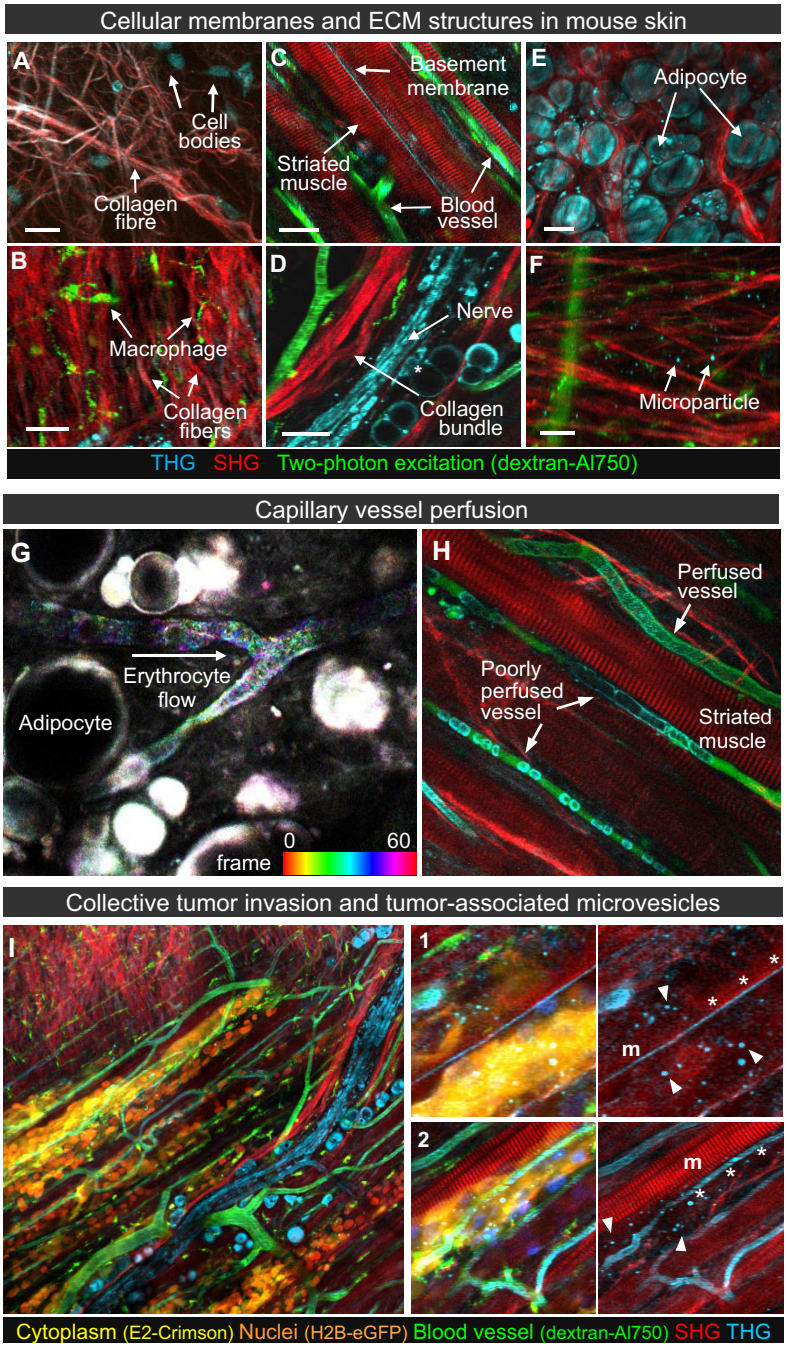

Fig. 3. Examples of tissue structures visualized *in vivo* by using THG. The diversity of the microanatomy of connective tissue (shown here, the mouse dermis) is visualized by combined THG, SHG and fluorescence imaging. Complementary to SHG and fluorescence, THG reveals collagen fibers and cell bodies in collagen-rich loose (A) and dense (B) interstitial tissue, basement membranes along myofibers and blood vessels (C), the multilayered myelination of peripheral nerves (D) and the surface of adipocytes (E). (F) In addition, THG-positive microparticles are detected, which drift through spaces between collagen fibers. Scale bars: 50 µm. Panels A–F are adapted from Alexander et al. (2013) with permission. (G) Erythrocyte flow in capillaries visualized by using THG. Shown here is a color-coded overlay of sequential images from a 1-min time-lapse sequence. Adapted from Weigelin et al. (2012). (H) Blood flow kinetics based on erythrocyte shape. The roundish shapes of immobile (lower vessel) or slowly moving erythrocytes (middle vessel) compared with a stripe-like THG pattern are the result of fast erythrocyte movement during image acquisition (upper vessel). The scanning direction was horizontal from left to right; this causes distortion of objects as they are moving during the scan. (I) B16F10 mouse melanoma cells invading into the dermis along muscle fibers ('m'). THG allows the visualization of the outer membrane of muscle fibers (asterisks, zoom 1) and perfused blood vessels, which serve as guidance structures for melanoma invasion (asterisks, zoom 2). In addition, THG-positive microvesicles are located in the interstitial space (arrowheads, zoom 1 and 2). Excitation conditions (all panels) – THG, SHG, dsRed, 1180 nm, 100 mW; GFP, AI750, 910 nm, 20 mW; backward detection.

2012). THG contrast in leukocytes primarily results from the plasma membrane and intracellular granules, which allows the identification of leukocyte subsets based on their differential granularity. Using this approach, it has been shown that neutrophils elicit a strong THG signal from intracellular granules, whereas lymphoid cells give rise to a preferential THG signal at cellular boundaries of hollow cores that resemble their large nucleus (Tsai et al., 2012). In addition, the polarity of moving leukocytes can be resolved easily owing to preferential redistribution of granules to the rear uropod (Fig. 2C; Movie 4). Thus, known cell subsets can be discriminated by using THG based on morphology and kinetic criteria, without the need for a fluorescent transgenic reporter strain.

Complementary to the visualization of cells, the THG signal originating from nuclear membranes (Fig. 2G) allows the characterization of shape, size and distribution of nuclei in tissues (Chu et al., 2005; Rehberg et al., 2011). Furthermore, chromocenters and heterochromatin structures are revealed in native tissue because of their different refractive indexes, without the need for DNA-intercalating stains (Rehberg et al., 2011). Exogenous application of acetic acid, which reversibly crosslinks nucleoproteins, can further enhance THG contrast in intact nuclei by changing their refractive index (Lee et al., 2007). This can be exploited to improve the detection of (pre-)cancerous lesions in mucosal tissues with optical biopsies, based on the presence of abnormalities in nuclear morphology and nucleocytoplasmic ratios that are typical for malignant cells (Lee et al., 2007; Tai et al., 2006; Tsai et al., 2011).

Blood vessel structure and function

Vascular biology is an emerging field of application for THG. Erythrocytes elicit a particularly strong THG signal that originates from their cellular membrane (Millard et al., 1999). An additional signal, with variable efficiency, originates from basement membranes lining the vessels (Rehberg et al., 2011; Weigelin et al., 2012). The resulting time-lapse THG recordings of erythrocyte flow kinetics reflect hemodynamic parameters, including blood flow velocity, the shear stress between erythrocytes and the vessel wall, and flow-deduced rates and rhythmicity of the heart beat (Dietzel et al., 2014) (Fig. 3G,H). In addition, resonance enhancement of the THG signal through distinct absorption maxima of oxy- and deoxyhemoglobin allows the simultaneous assessment of the level and pattern of blood oxygenation at cellular resolution (Chang et al., 2010b).

Cell-derived microvesicles

In addition to arising from intact cells, strong THG signals also originate from small cell-derived vesicles. In particular, cellular fragmentation during apoptosis generates cellular vesicles of variable sizes (Fig. 2E,F), but microvesicles are also shed by a variety of healthy cells, including tumor cells, and have been implicated in intercellular communication and oncogenic reprogramming of the local tumor microenvironment (Figs 2G and 3F,I) (Muralidharan-Chari et al., 2010; Zomer et al., 2015). In mouse melanoma lesions *in vivo*, extracellular tumor-associated microvesicles of variable size can be directly detected by using THG and followed in time (Weigelin et al., 2012). This has revealed at least three kinetic subsets of interstitial microvesicles, including stationary, slow diffusive and fast-moving vesicle subsets, and these properties might correlate with their function in conditioning cells and tissues locally and systemically (Weigelin et al., 2012).

Lipid bodies

Lipid bodies are ubiquitous structures involved in metabolic cellular functions and disorders of lipid biogenesis, and are associated with many human diseases, such as diabetes, cardiovascular diseases, obesity and cancer. Using THG, intracellular lipid body dynamics have revealed, for example, an altered metabolism that is defined by an increase in lipid body size and number in hepatocytes after partial hepatectomy (Débarre et al., 2006). Similarly, stage-dependent alterations of lipid deposits have been detected in *Caenorhabditis elegans* embryos and adult worms, including early-onset fat deposition during development followed by gradual reduction during aging, by using noninvasive long-term THG imaging (Tserevelakis et al., 2014). Similarly, THG time-lapse recordings in early mouse embryos have made it possible to observe the dynamics and aggregation kinetics of lipid droplets, and their movement, which depends on microtubules and microfilaments (Watanabe et al., 2010). Thus, alongside CARS, spontaneous Raman spectroscopy and lipophilic fluorescent dyes (Yen et al., 2010), THG also allows us to monitor the kinetics of fat metabolism and lipid storage.

Myofibers

Although SHG signals are elicited from ordered myosin in the A-bands of the sarcomere in striated myofibers, THG provides an alternating and complementary signal originating from the actin-rich I-bands between sarcomeres (Rehberg et al., 2010, 2011; Weigelin et al., 2012). THG provides label-free confocal 3D analyses of contracting striated myofibers and cardiomyocytes. By using cross-correlation with SHG and fluorescence, the kinetics of macro- and nanocontractions, related NADH levels, mitochondrial positioning and energy state can be determined (Barzda et al., 2005).

Brain and nervous system

To facilitate fast conduction of action potentials, nerves and axons in the central and peripheral nervous systems are surrounded by fatty myelin sheets. The multi-layered, lipid-rich membranes of the myelin sheaths that surround peripheral axons are a particularly strong source for THG (Fig. 3D,I) (Rehberg et al., 2011; Weigelin et al., 2012). In *ex vivo* and *in vivo* preparations of sciatic nerves of mice and rats, THG can be used to further resolve subdomains of myelinated peripheral nerves, including nodes of Ranvier, Schmidt–Lanterman incisures and Cajal bands. By using THG, myelination characteristics are amenable to rapid acquisition and bias-free automated quantification over large imaging fields (Lim et al., 2014). Therefore, THG might be useful to trace myelin loss and recovery in live tissue; for example, the degeneration of myelin sheets in multiple sclerosis, which causes deficits in sensory and motor functions of the demyelinated nerves. In the brain, THG signals correspond to regions of white matter, such as the mossy fibers in the cerebellar lobes, the pons and the hindbrain, and axon bundles in the corpus callosum (Farrar et al., 2011). Dense gray matter also produces THG, with a less intense and more homogeneous signal compared to that produced by white matter (Witte et al., 2011). The structural information provided by THG signals in neuronal tissue, and the possibility of being able to simultaneously visualize glass pipettes or small electrodes based on their strong refractive index, can guide the targeting of micropipettes to specific neurons for patch–clamp experiments or image-guided microsurgery applications (Witte et al., 2011). Taken together, these examples indicate that THG is a particularly promising approach to visualize changes in myelin organization *in vivo* during development and neurodegenerative diseases.

Virtual optical biopsy

Live-tissue analysis is an emerging field in clinical diagnostics, whereby image contrast is based on the application of exogenous

dyes, or absorption and endogenous fluorescence of human tissues. THG has the potential to complement these existing imaging approaches. The applicability of THG in optical biopsies has been demonstrated in hamster and human oral mucosa, as well as human skin and adipose tissue (Chen et al., 2009; Tai et al., 2005, 2006; Tsai et al., 2011, 2013). Furthermore, the image contrast generated using THG is suitable for discriminating melanoma and basal cell carcinoma lesions from normal skin and benign nevi (Chen et al., 2010). It has been shown that an abundant distribution of single cells or cell clusters with strongly enhanced THG intensity correlates with the morphology and melanin content of melanoma cells that have been identified in histological slices (Chen et al., 2010). THG could further be exploited to define the tumor margin during surgery or to verify the complete excision of the lesion in the removed tissue. Moreover, when THG has been used during heart surgery to assess the morphology, size and distribution of adipocytes, it has revealed a correlation between increased numbers of small-sized epicardial adipocytes and coronary artery disease (Tsai et al., 2013).

In recent clinical trials, the safety of THG for *in vivo* applications has been demonstrated. THG-based diagnosis of basal cell carcinoma *in vivo* depends upon the polymorphous variations in the size and shape of transformed cells, compared to normal tissue and the presence of peripheral palisading cells (Tsai et al., 2014). An increase in the size of cells and nuclei in intact skin are characteristics of aging tissue, which can be quantified *in vivo* based on THG analyses (Liao et al., 2013). By providing information on cell and tissue morphology in a label-free manner, THG thus generates diagnostic 3D information with a resolution comparable to that of traditional histopathology.

Abnormal vessel structures and altered hemodynamic factors are important parameters for diagnosing malignancies, and this has motivated the development of a miniaturized video-rate THG microscope for use in optical biopsies that has a sufficiently high spatial and temporal resolution to record blood flow in skin capillaries (Chia et al., 2010). Transcutaneous THG detection of blood cell flow in dermal capillaries of human volunteers is sensitive enough to capture blood flow dynamics, and the ratios of erythrocytes and white blood cells (Chen and Liu, 2012); this can be exploited for *in vivo* cytometry and hematological analysis without the need to draw blood. In malaria-infected blood cells, THG is particularly enhanced owing to the altered scatter properties that are caused by hemozoin, a parasite-derived pigment (Tripathy et al., 2013); this facilitates sensitive and rapid *ex vivo* detection of early stage infection in blood cells and thus has the potential to replace currently used skill- and time-intensive molecular analysis (Bélisle et al., 2008). The above studies clearly demonstrate the promise of THG to be used to detect interface changes at the microscale in the clinical diagnosis of various conditions.

Extracellular matrix and inorganic structures

Collagen and basement membranes

In addition to SHG, which originates from the core of fibrillar collagen, THG is excited from the surface of protein complexes, and delivers additional complementary detail and information regarding substructures. In thick collagen bundles and elastic fibers, THG is generated at the fiber surface and gives rise to a relief-like signal (Rehberg et al., 2011; Sun et al., 2007; Weigelin et al., 2012) (Figs 2G and 3A,B). Similarly, the outer membranes of myofibers and vessels induce THG, which is likely to originate from basement membrane structures (Rehberg et al., 2011; Weigelin et al., 2012) (Fig. 3C,H). Using combined SHG–THG imaging in late-stage melanoma that had been implanted in the mouse ear, it has been shown that significant collagen deposition and rearrangement of collagen structures occurs in parallel to expansive tumor growth (Wu et al., 2015). By generating a complementary signal to SHG (Fig. 2A,B), THG thus delivers consistent 3D information about healthy and diseased tissues at the subcellular level.

Bone and teeth

Inorganic crystals and mineralized complexes elicit strong THG signals owing to their high difference in refractive index compared to that of the surrounding tissue fluids. In mineralized bone, THG imaging allows the reconstruction of the outer and inner surfaces, which can be used to follow bone development in mouse embryos (Oron et al., 2004). In teeth, strong THG signals are produced by the calcified matrices of dentin and enamel, and have made it possible to highlight the dentinotubule structures and, to a lesser extent, the prismatic structures of enamel (Kao, 2004). By being able to detect dental discontinuities, such as cracks caused by thermal or mechanical stress, or white spot lesions as signs of mineral loss, THG is well suited for early diagnosis of enamel abnormalities (Chen et al., 2008). In paleontology research, teeth are the most abundant fossil material and contain key information about crucial biological functions, such as feeding and defense. Owing to its noninvasive nature, THG allows 3D reconstructions and morphometric analyses of dentinal structures without the need for histological preparation. These proof-of-concept results suggest that THG could contribute to classify the evolution of ancient vertebrate teeth without damaging rare fossils (Chen et al., 2015).

Combining THG and multimodal microscopy

To enhance current microscopy practice, THG can be combined with other multiphoton-excited fluorescence intensity signals or with fluorescence lifetime imaging (FLIM) within the same excitation and detection setup (Pelegati et al., 2012) (Box 1). For instance, multi-parameter approaches have combined label-free SHG and THG with fluorescence imaging (Fig. 3I). Furthermore, THG can also be used to correlate high-resolution electron microscopy with intravital imaging of molecules by detection with gold-labeled antibodies (Lippitz et al., 2005). Emerging key applications include the analysis of live cell–tissue interactions, cell dynamics in morphogenesis and cancer, vascular biology and organization of neuronal tissue.

Tissue dynamics in morphogenesis

The use of time-resolved 3D THG microscopy of transparent unstained zebrafish embryos until the 1000-cell stage has allowed reconstruction of a number of aspects of tissue kinetics with high detail, including imaging of the contour of the embryo, individual cell morphologies, yolk platelets and intracellular lipid vesicles (Olivier et al., 2010b). Combined with SHG – originating from mitotic spindles – and imaging of fluorescently labeled histone-2B of nuclear chromatin, the THG signal generated at cellular membranes allows measurement of the length of the cell cycle and of nucleocytoplasmic ratios, and enables lineage tracing over multiple cell divisions. Such tracing of cell cycle dynamics in time and space has shown that the cell cycle lengthens continuously, rather than abruptly, and that it is dependent on cell position and the embryo maturation stage (Olivier et al., 2010b). The THG signal originating from intracellular lipid bodies across the embryo can further be used for velocimetric analysis of morphogenetic movements, whereby the motion pattern of lipid bodies that are dispersed in the tissue are recorded to obtain a large-field map of

motion hotspots over time. Combined with fluorescence detection and local laser ablation of embryonic tissue structures, THG-based tracking of tissue structures (velocimetry) in *Drosophila* has shown that there is a long-ranging mechanical coupling of distant tissues, and that tissue and cell deformation correlates with the expression of the *twist* gene, a central regulator of *Drosophila* morphogenesis (Débarre et al., 2004; Supatto et al., 2005). Thus, the use of multimodal microscopy combined with THG can provide insights into tissue mechanics in a spatio-temporal manner.

Tumor–stroma interface

With respect to the tumor microenvironment, combination of THG with SHG and fluorescence detection has provided unprecedented details regarding tissue organization, cell–tissue interactions, blood flow dynamics and the dissemination of microvesicles (Weigelin et al., 2012). For instance, multispectral 3D reconstructions of early-stage melanoma lesions in the mouse dermis have identified the invasion strategies of melanoma cells, which depend on the type of tissue being invaded, as well as on tissue density and geometry. Collectively invading cells preferentially infiltrate tissue using a mechanism that is guided by confinement – i.e. the movement through pre-existing spaces along the interfaces of collagen bundles, myofibers, nerves and vessels (Weigelin et al., 2012) (Fig. 3I). In contrast, regions of tissue that comprise discontinuous fibrillar collagen-rich stroma support the dissemination of single cells or small clusters, suggesting that melanoma cells disperse in response to a loose organization of tissue. Quantification of tissue spaces before and after tumor invasion shows little tissue deformation and a lack of apparent structural degradation (Weigelin et al., 2012). This suggests a predominantly tissue-guided migration that is dictated by physical principles, including haptotaxis and contact guidance. By depicting the complexity of structural microenvironments *in vivo*, that study also provides the basis for bio-inspired engineered microdevices to probe cell migration in defined environments that simulate space restrictions, surface topography and geometry in the physiological range encountered by cells in tissues (Stroka et al., 2014; Yevick et al., 2015). Taken together, THG combined with SHG- or fluorescence-based microscopy can provide important anatomical context in three dimensions and so yield a framework of cause–consequence relationships in tumor progression, cell migration and the associated remodeling of the microenvironment.

Conclusions and outlook

By detecting cell and tissue interfaces in a noninvasive, label-free manner, THG fills the gap in resolution between mesoscale imaging, using OCT or high-resolution ultrasound, and nanoscopy that uses scanning electron microscopy to map the 3D tissue organization and function. Because of its ease of technical implementation in existing multiphoton imaging platforms and versatile application together with SHG and fluorescence imaging, THG shows great promise to emerge as a standard application of infrared multiphoton microscopy. Future *in vitro* applications in transparent samples will particularly benefit from collecting signals from forward THG and so help to address cell–matrix interactions in label-free samples, tissue remodeling and microvesicle biology in complex cell models. For intravital microscopy in small-animal models, THG is particularly useful when combined with chemical or genetically encoded probes. Promising fields of application include neuroscience, to address normal and perturbed microanatomy of central and peripheral neuronal tissue; material sciences, to monitor the 3D organization and tissue integration of engineered microdevices and biomaterials; vascular biology, for label-free detection of vascular anatomy and cell flow kinetics; and immunobiology and cancer research, to reveal tissue structures that guide and determine the positioning of cancer and immune cells. Furthermore, with the development of simpler, portable and more affordable devices, THG could enter clinical applications and field research. Here, areas of application include the optical biopsy of lipid organization and interfaces of body surfaces, dental disease – including the surface structure of teeth and tooth–tissue interfaces – and the analysis of diseased erythrocytes, such as after infection with malaria parasites. As an emerging field, optical THG-based tissue analysis will benefit from the development of microendoscopes, which will allow us to reach inner body surfaces and cavities. Thus, by enabling kinetic 3D analysis of tissue organization and function, THG will enhance both integrative 3D cell biology and preclinical and clinical ‘dynamic histopathology’.

Acknowledgements

We acknowledge Esther Wagena for outstanding assistance and technical support.

Competing interests

The authors declare no competing or financial interests.

Funding

This work was funded by the Dutch Cancer Foundation [grant number KWF 2008-4031]; FP7 of the European Union [grant number ENCITE HEALTH TH-15-2008-208142]; the Cancer Genomic Centre, The Netherlands; and the European Research Council consolidator grant DEEPINSIGHT.

Supplementary information

Supplementary information available online at
http://jcs.biologists.org/lookup/suppl/doi:10.1242/jcs.152272/-/DC1

References

Alexander, S., Weigelin, B., Winkler, F. and Friedl, P. (2013). Preclinical intravital microscopy of the tumour-stroma interface: invasion, metastasis, and therapy response. *Curr. Opin. Cell Biol.* **25**, 659-671.

Andresen, V., Alexander, S., Heupel, W.-M., Hirschberg, M., Hoffman, R. M. and Friedl, P. (2009). Infrared multiphoton microscopy: subcellular-resolved deep tissue imaging. *Curr. Opin. Biotechnol.* **20**, 54-62.

Aptel, F., Olivier, N., Deniset-Besseau, A., Legeais, J.-M., Plamann, K., Schanne-Klein, M.-C. and Beaurepaire, E. (2010). Multimodal nonlinear imaging of the human cornea. *Invest. Ophthalmol. Vis. Sci.* **51**, 2459-2465.

Barad, Y., Eisenberg, H., Horowitz, M. and Silberberg, Y. (1997). Nonlinear scanning laser microscopy by third harmonic generation. *Appl. Phys. Lett.* **70**, 922.

Barzda, V., Greenhalgh, C., Aus der Au, J., Elmore, S., van Beek, J. H. G. M., Squier, J., Van Beek, J. H. G. M. and Squier, J. (2005). Visualization of mitochondria in cardiomyocytes by simultaneous harmonic generation and fluorescence microscopy. *Opt. Express* **13**, 8263-8276.

Beard, P. (2011). Biomedical photoacoustic imaging: a review. *Interface Focus* **1**, 602-631.

Bélisle, J. M., Costantino, S., Leimanis, M. L., Bellemare, M.-J., Scott Bohle, D., Georges, E. and Wiseman, P. W. (2008). Sensitive detection of malaria infection by third harmonic generation imaging. *Biophys. J.* **94**, L26-L28.

Campagnola, P. J., Millard, A. C., Terasaki, M., Hoppe, P. E., Malone, C. J. and Mohler, W. A. (2002). Three-dimensional high-resolution second-harmonic generation imaging of endogenous structural proteins in biological tissues. *Biophys. J.* **82**, 493-508.

Chang, C.-F., Chen, H.-C., Chen, M.-J., Liu, W.-R., Hsieh, W.-F., Hsu, C.-H., Chen, C.-Y., Chang, F.-H., Yu, C.-H. and Sun, C.-K. (2010a). Direct backward third-harmonic generation in nanostructures. *Opt. Express* **18**, 7397-7406.

Chang, C.-F., Yu, C.-H. and Sun, C.-K. (2010b). Multi-photon resonance enhancement of third harmonic generation in human oxyhemoglobin and deoxyhemoglobin. *J. Biophotonics* **3**, 678-685.

Chen, C.-K. and Liu, T.-M. (2012). Imaging morphodynamics of human blood cells in vivo with video-rate third harmonic generation microscopy. *Biomed. Opt. Express* **3**, 2860-2865.

Chen, I.-H., Chu, S.-W., Sun, C.-K., Cheng, P.-C. and Lin, B.-L. (2002). Wavelength dependent damage in biological multi-photon confocal microscopy: a micro-spectroscopic comparison between femtosecond Ti:sapphire and Cr: forsterite laser sources. *Opt. Quantum Electron.* **34**, 1251-1266.

Chen, S.-Y., Hsu, C.-Y. and Sun, C.-K. (2008). Epi-third and second harmonic generation microscopic imaging of abnormal enamel. *Opt. Express* **16**, 11670-11679.
Chen, S.-Y., Wu, H.-Y. and Sun, C.-K. (2009). In vivo harmonic generation biopsy of human skin. *J. Biomed. Opt.* **14**, 060505.
Chen, S.-Y., Chen, S.-U., Wu, H.-Y., Lee, W.-J., Liao, Y.-H. and Sun, C.-K. (2010). In vivo virtual biopsy of human skin by using noninvasive higher harmonic generation microscopy. *IEEE J. Sel. Top. Quantum Electron.* **16**, 478-492.
Chen, Y.-C., Lee, S.-Y., Wu, Y., Brink, K., Shieh, D.-B., Huang, T. D., Reisz, R. R. and Sun, C.-K. (2015). Third-harmonic generation microscopy reveals dental anatomy in ancient fossils. *Opt. Lett.* **40**, 1354-1357.
Cheng, J.-X. and Xie, X. S. (2002). Green's function formulation for third-harmonic generation microscopy. *J. Opt. Soc. Am. B* **19**, 1604.
Cheng, L.-C., Horton, N. G., Wang, K., Chen, S.-J. and Xu, C. (2014). Measurements of multiphoton action cross sections for multiphoton microscopy. *Biomed. Opt. Express* **5**, 3427.
Chia, S.-H., Yu, C., Lin, C., Cheng, N., Liu, T., Chan, M.-C., Chen, I. and Sun, C.-K. (2010). Miniaturized video-rate epi-third-harmonic-generation fiber-microscope. *Opt. Express* **18**, 17382-17391.
Chu, S.-W., Chen, I.-H., Liu, T.-M., Sun, C.-K., Lee, S.-P., Lin, B.-L., Cheng, P.-C., Kuo, M.-X., Lin, D.-J. and Liu, H.-L. (2002). Nonlinear bio-photonic crystal effects revealed with multimodal nonlinear microscopy. *J. Microsc.* **208**, 190-200.
Chu, S.-W., Chen, S.-Y., Tsai, T.-H., Liu, T., Lin, C.-Y., Tsai, H.-J. and Sun, C.-K. (2003). In vivo developmental biology study using noninvasive multi-harmonic generation microscopy. *Opt. Express* **11**, 3093-3099.
Chu, S.-W., Tai, S.-P., Ho, C.-L., Lin, C.-H. and Sun, C.-K. (2005). High-resolution simultaneous three-photon fluorescence and third-harmonic-generation microscopy. *Microsc. Res. Tech.* **66**, 193-197.
Débarre, D., Supatto, W., Farge, E., Moulia, B., Schanne-Klein, M.-C. and Beaurepaire, E. (2004). Velocimetric third-harmonic generation microscopy: micrometer-scale quantification of morphogenetic movements in unstained embryos. *Opt. Lett.* **29**, 2881-2883.
Débarre, D., Supatto, W. and Beaurepaire, E. (2005). Structure sensitivity in third-harmonic generation microscopy. *Opt. Lett.* **30**, 2134-2136.
Débarre, D., Supatto, W., Pena, A.-M., Fabre, A., Tordjmann, T., Combettes, L., Schanne-Klein, M.-C. and Beaurepaire, E. (2006). Imaging lipid bodies in cells and tissues using third-harmonic generation microscopy. *Nat. Methods* **3**, 47-53.
Débarre, D., Olivier, N. and Beaurepaire, E. (2007). Signal epidetection in third-harmonic generation microscopy of turbid media. *Opt. Express* **15**, 8913-8924.
Débarre, D., Olivier, N., Supatto, W. and Beaurepaire, E. (2014). Mitigating phototoxicity during multiphoton microscopy of live drosophila embryos in the 1.0–1.2 µm wavelength range. *PLoS ONE* **9**, e104250.
Dietzel, S., Pircher, J., Nekolla, A. K., Gull, M., Brändli, A. W., Pohl, U. and Rehberg, M. (2014). Label-free determination of hemodynamic parameters in the microcirculaton with third harmonic generation microscopy. *PLoS ONE* **9**, e99615.
Drexler, W., Liu, M., Kumar, A., Kamali, T., Unterhuber, A. and Leitgeb, R. A. (2014). Optical coherence tomography today: speed, contrast, and multimodality. *J. Biomed. Opt.* **19**, 071412.
Ellenbroek, S. I. J. and van Rheenen, J. (2014). Imaging hallmarks of cancer in living mice. *Nat. Rev. Cancer* **14**, 406-418.
Evans, C. L. and Xie, X. S. (2008). Coherent anti-stokes raman scattering microscopy: chemical imaging for biology and medicine. *Annu. Rev. Anal. Chem.* **1**, 883-909.
Farrar, M. J., Wise, F. W., Fetcho, J. R. and Schaffer, C. B. (2011). In vivo imaging of myelin in the vertebrate central nervous system using third harmonic generation microscopy. *Biophys. J.* **100**, 1362-1371.
Fereidouni, F., Bader, A. N., Colonna, A. and Gerritsen, H. C. (2014). Phasor analysis of multiphoton spectral images distinguishes autofluorescence components of in vivo human skin. *J. Biophotonics* **7**, 589-596.
Franken, P. A., Hill, A. E., Peters, C. W. and Weinreich, G. (1961). Generation of optical harmonics. *Phys. Rev. Lett.* **7**, 118-119.
Friedl, P., Wolf, K., von Andrian, U. H. and Harms, G. (2007). Biological second and third harmonic generation microscopy. *Curr. Protoc. Cell Biol.* Chapter 4, Unit 4.15.
Helmchen, F. and Denk, W. (2005). Deep tissue two-photon microscopy. *Nat. Methods* **2**, 932-940.
Horton, N. G., Wang, K., Kobat, D., Clark, C. G., Wise, F. W., Schaffer, C. B. and Xu, C. (2013). In vivo three-photon microscopy of subcortical structures within an intact mouse brain. *Nat. Photonics* **7**, 205-209.
Jay, L., Bourget, J.-M., Goyer, B., Singh, K., Brunette, I., Ozaki, T. and Proulx, S. (2015). Characterization of tissue-engineered posterior corneas using second- and third-harmonic generation microscopy. *PLoS ONE* **10**, e0125564.
Kao, F.-J. (2004). The use of optical parametric oscillator for harmonic generation and two-photon UV fluorescence microscopy. *Microsc. Res. Tech.* **63**, 175-181.
Lee, W.-J., Yu, C.-H., Tai, S.-P., Huang, H.-Y. and Sun, S.-K. (2007). Acetic acid as a cell nucleus contrast agent in third-harmonic generation microscopy. *J. Med. Biol. Eng.* **27**, 161-164.
Liao, Y.-H., Chen, S.-Y., Chou, S.-Y., Wang, P.-H., Tsai, M.-R. and Sun, C.-K. (2013). Determination of chronological aging parameters in epidermal keratinocytes by in vivo harmonic generation microscopy. *Biomed. Opt. Express* **4**, 77-88.
Lim, H., Sharoukhov, D., Kassim, I., Zhang, Y., Salzer, J. L. and Melendez-Vasquez, C. V. (2014). Label-free imaging of Schwann cell myelination by third harmonic generation microscopy. *Proc. Natl. Acad. Sci. USA* **111**, 18025-18030.
Lippitz, M., van Dijk, M. A., Orrit, M., Dijk, M. A. and Orrit, M. (2005). Third-harmonic generation from single gold nanoparticles. *Nano Lett.* **5**, 799-802.
Mahou, P., Olivier, N., Labroille, G., Duloquin, L., Sintes, J.-M., Peyriéras, N., Legouis, R., Débarre, D. and Beaurepaire, E. (2011). Combined third-harmonic generation and four-wave mixing microscopy of tissues and embryos. *Biomed. Opt. Express* **2**, 2837-2849.
McConnell, G. (2006). Improving the penetration depth in multiphoton excitation laser scanning microscopy. *J. Biomed. Opt.* **11**, 054020.
Millard, A. C., Wiseman, P. W., Fittinghoff, D. N., Wilson, K. R., Squier, J. A. and Müller, M. (1999). Third-harmonic generation microscopy by use of a compact, femtosecond fiber laser source. *Appl. Opt.* **38**, 7393-7397.
Müller, M., Squier, J., Wilson, K. and Brakenhoff, G. (1998). 3D microscopy of transparent objects using third-harmonic generation. *J. Microsc.* **191**, 266-274.
Muralidharan-Chari, V., Clancy, J. W., Sedgwick, A. and D'Souza-Schorey, C. (2010). Microvesicles: mediators of extracellular communication during cancer progression. *J. Cell Sci.* **123**, 1603-1611.
Olivier, N., Aptel, F., Plamann, K., Schanne-Klein, M.-C. and Beaurepaire, E. (2010a). Harmonic microscopy of isotropic and anisotropic microstructure of the human cornea. *Opt. Express* **18**, 5028-5040.
Olivier, N., Luengo-Oroz, M. A., Duloquin, L., Faure, E., Savy, T., Veilleux, I., Solinas, X., Débarre, D., Bourgine, P., Santos, A. et al. (2010b). Cell lineage reconstruction of early zebrafish embryos using label-free nonlinear microscopy. *Science* **329**, 967-971.
Oron, D., Yelin, D., Tal, E., Raz, S., Fachima, R. and Silberberg, Y. (2004). Depth-resolved structural imaging by third-harmonic generation microscopy. *J. Struct. Biol.* **147**, 3-11.
Pelegati, V. B., Adur, J., De Thomaz, A. A., Almeida, D. B., Baratti, M. O., Andrade, L. A. L. A., Bottcher-luiz, F. and Cesar, C. L. (2012). Harmonic optical microscopy and fluorescence lifetime imaging platform for multimodal imaging. *Microsc. Res. Tech.* **75**, 1383-1394.
Rehberg, M., Krombach, F., Pohl, U. and Dietzel, S. (2010). Signal improvement in multiphoton microscopy by reflection with simple mirrors near the sample. *J. Biomed. Opt.* **15**, 026017.
Rehberg, M., Krombach, F., Pohl, U. and Dietzel, S. (2011). Label-free 3D visualization of cellular and tissue structures in intact muscle with second and third harmonic generation microscopy. *PLoS ONE* **6**, e28237.
Skala, M. C., Riching, K. M., Bird, D. K., Gendron-Fitzpatrick, A., Eickhoff, J., Eliceiri, K. W., Keely, P. J. and Ramanujam, N. (2007). In vivo multiphoton fluorescence lifetime imaging of protein-bound and free nicotinamide adenine dinucleotide in normal and precancerous epithelia. *J. Biomed. Opt.* **12**, 024014.
Squier, J., Muller, M., Brakenhoff, G. and Wilson, K. R. (1998). Third harmonic generation microscopy. *Opt. Express* **3**, 315-324.
Stroka, K. M., Gu, Z., Sun, S. X. and Konstantopoulos, K. (2014). Bioengineering paradigms for cell migration in confined microenvironments. *Curr. Opin. Cell Biol.* **30**, 41-50.
Sun, C.-K., Chu, S.-W., Chen, S.-Y., Tsai, T.-H., Liu, T.-M., Lin, C.-Y. and Tsai, H.-J. (2004). Higher harmonic generation microscopy for developmental biology. *J. Struct. Biol.* **147**, 19-30.
Sun, C.-K., Yu, C.-H., Tai, S.-P., Kung, C.-T., Wang, I.-J., Yu, H.-C., Huang, H.-J., Lee, W.-J. and Chan, Y.-F. (2007). In vivo and ex vivo imaging of intra-tissue elastic fibers using third-harmonic-generation microscopy. *Opt. Express* **15**, 11167-11177.
Supatto, W., Débarre, D., Moulia, B., Brouzés, E., Martin, J.-L., Farge, E. and Beaurepaire, E. (2005). In vivo modulation of morphogenetic movements in Drosophila embryos with femtosecond laser pulses. *Proc. Natl. Acad. Sci. USA* **102**, 1047-1052.
Tai, S.-P., Tsai, T.-H., Lee, W.-J., Shieh, D.-B., Liao, Y.-H., Huang, H.-Y., Zhang, K. Y.-J., Liu, H.-L. and Sun, C.-K. (2005). Optical biopsy of fixed human skin with backward-collected optical harmonics signals. *Opt. Express* **13**, 8231-8242.
Tai, S.-P., Lee, W.-J., Shieh, D.-B., Wu, P.-C., Huang, H.-Y., Yu, C.-H. and Sun, C.-K. (2006). In vivo optical biopsy of hamster oral cavity with epi-third-harmonic-generation microscopy. *Opt. Express* **14**, 6178-6187.
Thayil, A., Watanabe, T., Jesacher, A., Wilson, T., Srinivas, S. and Booth, M. (2011). Long-term imaging of mouse embryos using adaptive harmonic generation microscopy. *J. Biomed. Opt.* **16**, 046018.
Tripathy, U., Giguère-Bisson, M., Sangji, M. H., Bellemare, M.-J., Bohle, D. S., Georges, E. and Wiseman, P. W. (2013). Optimization of malaria detection based on third harmonic generation imaging of hemozoin. *Anal. Bioanal. Chem.* **405**, 5431-5440.
Tsai, M.-R., Chen, S.-Y., Shieh, D.-B., Lou, P.-J. and Sun, C.-K. (2011). In vivo optical virtual biopsy of human oral mucosa with harmonic generation microscopy. *Biomed. Opt. Express* **2**, 2317-2328.
Tsai, C.-K., Chen, Y.-S., Wu, P.-C., Hsieh, T.-Y., Liu, H.-W., Yeh, C.-Y., Lin, W.-L., Chia, J.-S. and Liu, T.-M. (2012). Imaging granularity of leukocytes with third harmonic generation microscopy. *Biomed. Opt. Express* **3**, 2234-2243.

Journal of Cell Science

Tsai, C.-K., Wang, T.-D., Lin, J.-W., Hsu, R.-B., Guo, L.-Z., Chen, S.-T. and Liu, T.-M. (2013). Virtual optical biopsy of human adipocytes with third harmonic generation microscopy. *Biomed. Opt. Express* **4**, 178-186.

Tsai, M.-R., Cheng, Y.-H., Chen, J.-S., Sheen, Y.-S., Liao, Y.-H. and Sun, C.-K. (2014). Differential diagnosis of nonmelanoma pigmented skin lesions based on harmonic generation microscopy. *J. Biomed. Opt.* **19**, 036001.

Tserevelakis, G. J., Megalou, E. V., Filippidis, G., Petanidou, B., Fotakis, C. and Tavernarakis, N. (2014). Label-free imaging of lipid depositions in C. elegans using third-harmonic generation microscopy. *PLoS ONE* **9**, e84431.

Watanabe, T., Thayil, A., Jesacher, A., Grieve, K., Debarre, D., Wilson, T., Booth, M. and Srinivas, S. (2010). Characterisation of the dynamic behaviour of lipid droplets in the early mouse embryo using adaptive harmonic generation microscopy. *BMC Cell Biol.* **11**, 38.

Weigelin, B., Bakker, G.-J. and Friedl, P. (2012). Intravital third harmonic generation microscopy of collective melanoma cell invasion: principles of interface guidance and microvesicle dynamics. *Intravital* **1**, 32-43.

Witte, S., Negrean, A., Lodder, J. C., de Kock, C. P. J., Testa Silva, G., Mansvelder, H. D. and Louise Groot, M. (2011). Label-free live brain imaging and targeted patching with third-harmonic generation microscopy. *Proc. Natl. Acad. Sci. USA* **108**, 5970-5975.

Wu, P.-C., Hsieh, T.-Y., Tsai, Z.-U. and Liu, T.-M. (2015). In vivo quantification of the structural changes of collagens in a melanoma microenvironment with second and third harmonic generation microscopy. *Sci. Rep.* **5**, 8879.

Yelin, D. and Silberberg, Y. (1999). Laser scanning third-harmonic-generation microscopy in biology. *Opt. Express* **5**, 169-175.

Yelin, D., Silberberg, Y., Barad, Y. and Patel, J. S. (1999). Depth-resolved imaging of nematic liquid crystals by third-harmonic microscopy. *Appl. Phys. Lett.* **74**, 3107.

Yen, K., Le, T. T., Bansal, A., Narasimhan, S. D., Cheng, J.-X. and Tissenbaum, H. A. (2010). A comparative study of fat storage quantitation in nematode Caenorhabditis elegans using label and label-free methods. *PLoS ONE* **5**, e12810.

Yevick, H. G., Duclos, G., Bonnet, I. and Silberzan, P. (2015). Architecture and migration of an epithelium on a cylindrical wire. *Proc. Natl. Acad. Sci. USA* **112**, 5944-5949.

Zhang, Y. S., Wang, L. V. and Xia, Y. (2015). Seeing through the surface: non-invasive characterization of biomaterial–tissue interactions using photoacoustic microscopy. *Ann. Biomed. Eng.* [Epub ahead of print]. doi:10.1007/s10439-015-1485-2

Zimmerley, M., Mahou, P., Débarre, D., Schanne-Klein, M. C. and Beaurepaire, E. (2013). Probing ordered lipid assemblies with polarized third-harmonic-generation microscopy. *Phys. Rev. X* **3**, 011002.

Zipfel, W. R., Williams, R. M. and Webb, W. W. (2003). Nonlinear magic: multiphoton microscopy in the biosciences. *Nat. Biotechnol.* **21**, 1369-1377.

Zomer, A., Maynard, C., Verweij, F. J., Kamermans, A., Schäfer, R., Beerling, E., Schiffelers, R. M., de Wit, E., Berenguer, J., Ellenbroek, S. I. J. et al. (2015). In vivo imaging reveals extracellular vesicle-mediated phenocopying of metastatic behavior. *Cell* **161**, 1046-1057.